Programmable Metasurface Antenna for Electromagnetic Torso Scanning

AMIN DARVAZEHBAN[ID], **(Student Member, IEEE), SASAN AHDI REZAEIEH**[ID]**, (Member, IEEE), AND AMIN M. ABBOSH**[ID]**, (Senior Member, IEEE)**
School of Information Technology and Electrical Engineering, The University of Queensland, QLD 4072, Australia

Corresponding author: Amin Darvazehban (a.darvazehban@uq.edu.au)

ABSTRACT A wideband beam-switching metasurface antenna using programmable unit-cells is proposed for electromagnetic torso scanning. The design aims at changing the intensity of the electric field inside the torso without any mechanical movements and thus enables fast electronic scanning of the torso. The antenna consists of an H-shape microstrip-fed slot as the radiator and a metasurface layer containing 5×5 programmable square ring resonator as the superstrate layer. Four PIN diodes are embedded in each cell to alter the electric field intensity within the metasurface layer and consequently switch the radiation pattern in the azimuth plane, elevation plane, and diagonal axis of the metasurface layer. As a proof of concept, a prototype antenna capable of switching the radiation pattern from $-25°$ to $+25°$ in the azimuth (x-z) plane is fabricated and measured. The antenna, which has the compact size of $0.9\lambda_0 \times 0.9\lambda_0 \times 0.06\lambda_0$ (where λ_0 is the wavelength at the center operation frequency), achieves a wide bandwidth of 30% at 0.9–1.2 GHz. The peak measured gain is 9.5 dBi with maximum front to back ratio of 12 dB. The fabricated antenna is successfully tested on altering the intensity of the electric field at right, center and left sides of a torso phantom.

INDEX TERMS Pattern reconfigurable antenna, metasurfaces, torso scanner, electronic beam switching.

I. INTRODUCTION

Pleural effusion and pulmonary edema are the common manifestations behind various diseases such as heart failure, liver disorder, blood clots and kidney diseases [1] that lead to accumulation of fluid inside or around the lungs. Hence, causing difficulties in breathing and other complications that can led to sever damage to vital organs in the body. Currently, X-ray devices are the most popular diagnostic tool to detect the fluid accumulation. However, they suffer from ionizing radiation that require shielding equipment, hence, cannot be widely used in clinics Moreover, due to safety regulations, they cannot be performed regularly for monitoring purposes. To alleviate this problem, non-ionizing electromagnetic imaging (EMI) systems were proposed and successfully tested in recent years [2]–[4]. EMI systems have the advantages of being non-invasive, low-cost, low profile, portable, and can be used for frequent monitoring of the disease. The

The associate editor coordinating the review of this manuscript and approving it for publication was Shah Nawaz Burokur[ID].

operation principle of these systems is based on the existing contrast in the dielectric properties of the healthy and malignant tissue, e.g. liver and fluid [5]–[9]. This contrast alters the amplitude and/or phase of the electromagnetic signal and consequently the intensity of the scattered electric field.

Antennas have the essential role of transmitting the electromagnetic signals into the targeted area and receiving the reflected/scattered signals. Depending on the utilized post-processing technique, generally different scattered profiles at different frequency samples of a wideband signal within 0.5-1 GHz is used in the processing and image creation to compensate for the small number of discrete observation points [10], [11]. Moreover, due to the limited allowed power, unidirectional antennas with high front-to-back ratio (FBR) are preferred in EMI systems for better signal penetration and reduced external interference [12].

Different types of antennas with fixed unidirectional radiation have been proposed for EMI systems [12]–[17]. Stacked patch antenna [12], metasurfaces [16], Vivaldi antenna [13], dielectric resonator antenna (DRA) [14], and planar Yagi

antennas [15] are among the most popular antennas for EMI systems. Despite their notable performance, their main limitation is the fixed radiation pattern. Therefore, to scan different parts of the torso area, an array of antennas along the torso or a mechanically movable structure is needed [3], [18]. Hence, resulting in a complex and bulky system that is prone to mechanical movement errors. To avoid that limitation, pattern reconfigurable antennas can be used as the scanning platform. Traditional beam switching techniques such as beamforming networks [19], [20], lens structures [21], [22] and phased arrays [23], [24], are effective. Yet, they increase the complexity and size of the system, especially at lower microwave frequencies.

Pattern reconfigurability can be achieved using partially reflective surfaces (PRS) antennas [25], [26], metasurfaces [27]–[30], and reflect/transmit arrays [31]–[33]. The PRS antenna presented in [25] is fed by a small phased array antenna, requiring complex beamforming network for feeding. The pattern reconfigurability in [27] is achieved by horizontally shifting the location of the radiating slots using offsetting technique. The same concept is utilized in [28] by activating/deactivating each radiating slot using PIN diodes. The main drawbacks of using the offsetting techniques are: 1) increased number of half wavelength radiating slots and feeding lines to achieve beam re-configurability that increases the size of antenna, 2) adverse effect of surface current from adjacent slots on the radiated beam, and 3) increased complexity of feeding network for 2-D beam steering in the azimuth and elevation planes. The Transmit/Reflect arrays are intrinsically narrowband such as the reconfigurable reflectarray presented in [31] achieves maximum scanning angle of 18.3° in a narrow bandwidth of 5.8% from 10.1GHz to 10.7 GHz.

To overcome these limitations, a low-profile beam switching metasurface antenna with a simple switching network is presented. The antenna consists of a microstrip-fed H-shape radiating slot that radiates via a programmable metasurface superstrate layer. Programmable means that by activating/deactivating each row/column of cells, different scenarios of pattern reconfigurability can be achieved. The H-shape slot achieves wider bandwidth and higher radiation efficiency than the traditional rectangular slot [34]. Size of the proposed metasurface layer is set to cover an average human torso, which results in a 5×5 programmable unit cells. Four PIN diodes are embedded across each unit cell to deactivate each cell. By deactivating each column/row of the unit cells, the electric field density across the metasurface layer changes and consequently, the beam is switched to the designed direction. A prototype is fabricated and tested. The antenna achieves a wide fractional bandwidth of 30% at 0.9 −1.2 GHz with a compact size of $0.9\lambda_0 \times 0.9\lambda_0 \times 0.06\lambda_0$ (where $\lambda_0\lambda_0$ is the wavelength at the center operation frequency). The radiation pattern can be switched from −25° to 0° and +25° in both the azimuth and the elevation planes. The antenna is successfully tested to alter the intensity of the electric field at different directions inside a torso phantom.
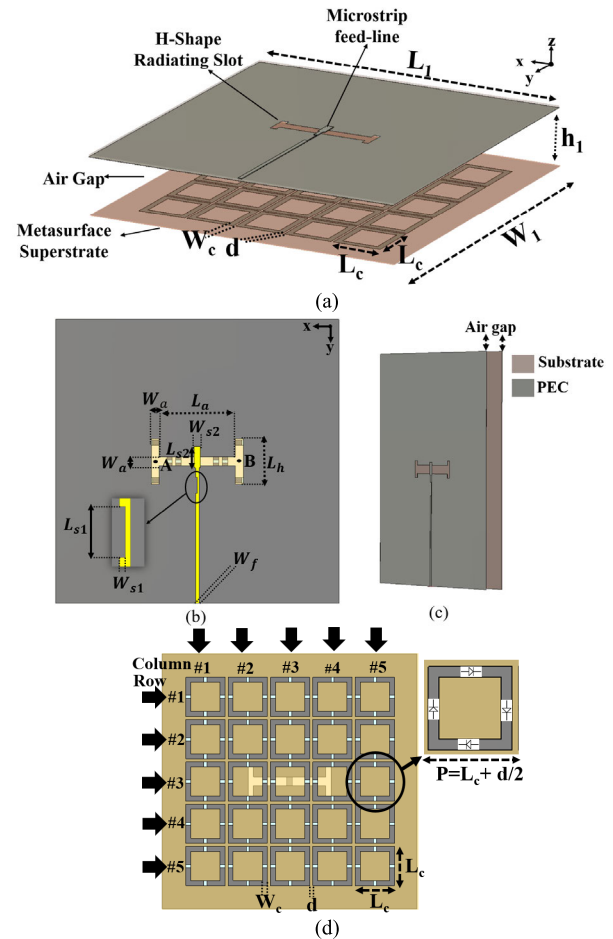

FIGURE 1. Configuration of the proposed antenna: a) Perspective view, b) H-Shaped microstrip fed radiating slot, c) side view, and d) metasurface Superstrate. L1 = W1= 250, h1= 20, La = 70, Wa = 8, Lh = 35, Ls1 = 14.2, Ws1 = 2, Ls2 = 8.2, Ws1 = 5, Wf = 3.05, Lc = 38, Wc = 4.5, d = 2 (mm).

II. ANTENNA DESIGN AND DISCUSSION

The configuration of the proposed antenna is depicted in Fig. 1. The antenna consists of an H-shape microstrip-fed radiating slot printed on an FR-4 substrate with the dielectric constant of 4.4, loss tangent of 0.02 and thickness of 1.6 millimeters, illuminating a layer of metasurface superstrate. The metasurface layer contains 5×5 square ring resonator (SRR) unit cells fabricated on an FR-4 substrate with a thickness of 0.8 mm. Four plastic screws are used to adjust the air-gap (h_1) between the radiating slot and the metasurface superstrate layer. Four PIN diodes are embedded across each unit cell on four arms to control the wave on horizontal and vertical directions of the metasurface layer and change the electric field densities within that layer. Different electric field distributions and consequently beam directions can be achieved by activating/deactivating the cells of different columns and rows. To avoid using matching medium between the antenna and the human torso, the antenna is designed in free space. The differences between the performance of S-parameters in free space and in front of the human torso can then be used for boundary estimation and detection. The

electromagnetic torso scanning system operating in the low microwave frequency band involves both near- and far-field propagation problems. Thus, the overall scattered fields are a combination of both. Therefore, to simplify the problem, far-field radiation as the dominant element is assumed when running the algorithm. This is actually a reasonable assumption; the near/far-field in the utilized algorithm is defined based on the radiating near-field region ($r > 0.62\sqrt{\frac{D^3}{\lambda}}$) and far-field ($r > \frac{2D^2}{\lambda}$) region, where D is the effective diameter of the antenna, and λ is the effective wavelength at the center frequency. For the investigated torso abnormalities with an average human torso size that has average dielectric constant around 40, any distance up to 5 cm inside the torso is within the radiating near-field and then antenna operates dominantly within the far-field. This assumption is being widely used for microwave imaging systems [35], [36].

A. RADIATING SLOT

Since the electric field distribution across an H-shape slot is more uniform than a rectangular slot, the H-shape radiating slot is used as the radiating element resulting in a widened bandwidth, increased radiation efficiency and reduced back radiation [34]. The width of the slot is selected to be small relative to the guided-wavelength at the center frequency ($W_a = 0.02\lambda_g$) to reduce the electric field in the direction of slot axis, and consequently reduce the cross-polarized radiation [37], [38]. For a reasonably uniform field across the lateral slot, its length is selected to be around half of the guided wavelength, whereas the perpendicular slots at its edges are chosen to be around a quarter guided wavelength [39]. The distribution of the electric field across the slot at the center frequency of 1.05 GHz for H-shape slot and rectangular slot is shown in Fig. 2. As illustrated in Fig. 2, the conventional rectangular slot has a sinusoidal electric field distribution with minimum intensity at point A and B of the slot ends (see Fig. 1(b)). However, the end-loaded H-shape slot increases the level of the electric field these points. As a result, the field distribution becomes more uniform [39]. An open-ended matching stub with dimensions of $L_{s1} \times W_{s1}$ is added to the 50Ω microstrip feed line to reduce the adverse inductive behavior of the antenna (see Fig. 3 (a)-(b)). Moreover, to improve the electromagnetic coupling between the microstrip feed line and H-shape radiating slot, another stub with dimensions of $L_{s2} \times W_{s2}$ is added to the end of 50Ω microstrip feed line. Final dimensions of the H-shape slot and the open-ended matching stub are obtained using particle swarm optimization (PSO) method in CST Microwave studio and are presented in caption of Fig. 1.

B. METASURFACE LAYER

A simple symmetric closed sub-wavelength SRR [27] is used as the unit cell for the metasurface layer. Four PIN diodes are used across the cell, where one diode is located on each arm, to activate/deactivate each cell. The procedure for calculating
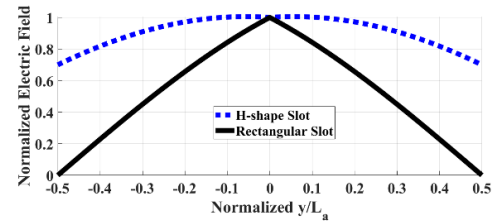

FIGURE 2. Comparison between electric field distribution across the slot for H-shape slot and rectangular slot at the center frequency of 1.05 GHz.
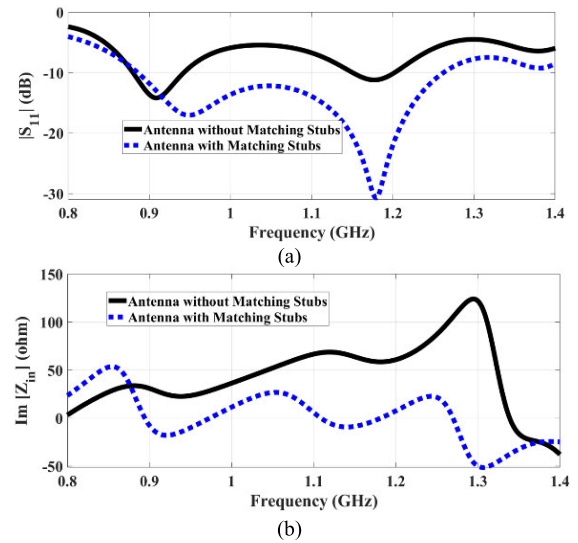

FIGURE 3. Effect of adding matching stub on the performance of the proposed antenna: a) |S11|, and b) Imaginary parts of input impedance.

the dimensions of an SRR is discussed in [40]. By setting the operational frequency and the width of the cell as fraction of guided-wavelength at the center frequency (W_c/λ_g) as the known values, the length of the unit cell (L_c) and the periodicity (P) can be calculated as [40]:

$$1 = 4\left(\frac{L_c}{\lambda_g}\right)^2 \times \ln\left(\frac{2M\lambda_g}{\pi W_c}\right) \tag{1}$$

and

$$P = M\lambda_g, \tag{2}$$

where M is a constant that varies at 0 - 1. CST Microwave Studio is then used to analyze and optimize the resonance frequency of the unit cell, which has the final dimensions of $L_c = 38$ mm, $W_c = 4.5$ mm, and $d = 2$ mm. Additionally, a unit-cell analysis is performed to calculate its effective permittivity (ε_{eff}) and effective permeability (μ_{eff}) in two different operating modes using the retrieval process [41]. The unit cell is simulated in CST Microwave studio with the unit cell boundary condition in *x* and *y* directions and open boundary condition in *z* direction (See Fig. 4(a)). The calculated effective permittivity and effective permeability at two different operating *States* when all diodes are ON (Fig. 4(b)) and all diodes are OFF (Fig. 4(c)) are presented in
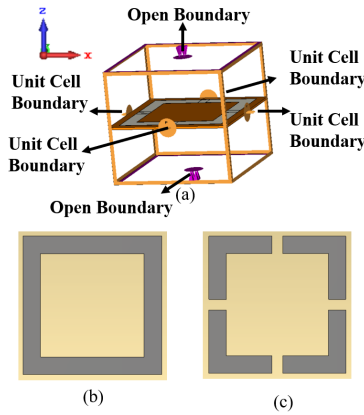
FIGURE 4. Unit cell simulation. a) simulation setup, b) unit cell when all diodes are ON, and c) unit cell when all diodes are OFF.
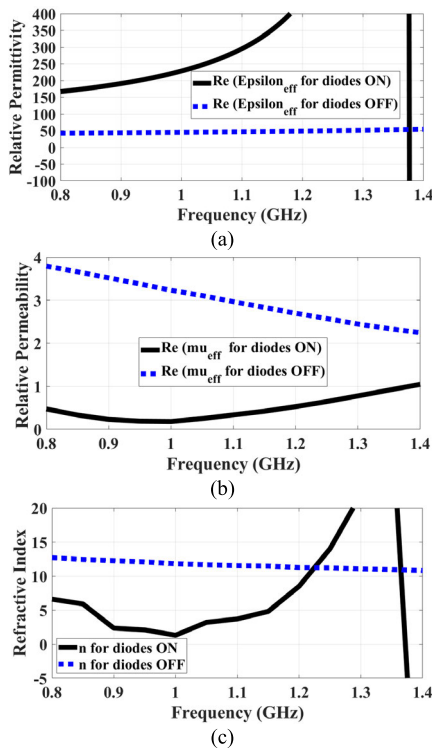

FIGURE 5. Effective permeability and permittivity of the unit cell when all diodes are ON or OFF: a) Relative permittivity, b) relative permeability and c) refractive index.

Fig. 5. When all PIN diodes are *ON*, the effective permeability of the cell approaches to zero at the operating bandwidth of 0.8-1.2 GHz, indicating the mu-near-zero (MNZ) material state. On the other hand, when the unit cell is deactivated by turning the PIN diodes *OFF*, the effective permeability increases, and consequently the effectiveness of the metasurface as a superstrate in front of the radiating slot decreases. Gain enhancement and bandwidth improvement can be achieved using MNZ by creating a near-zero refractive index (NZRI) medium in front of the incident wave-front. Based on Snell's law, the NZRI collimates the electromagnetic energy into a focal point in front of the antenna and
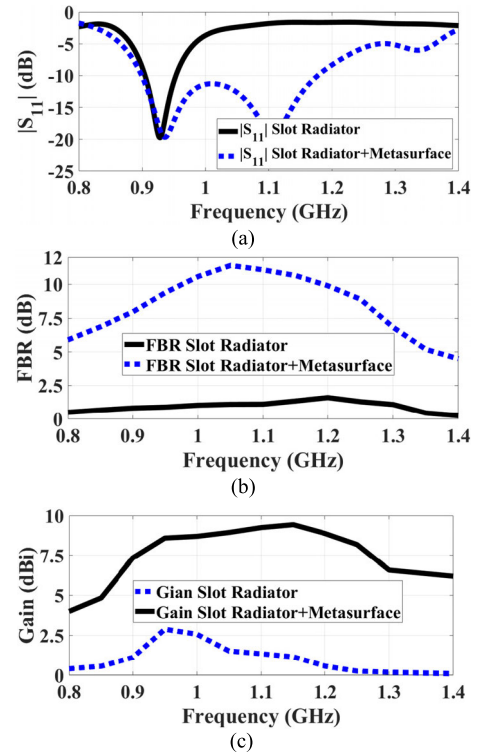

FIGURE 6. Comparison between slot radiator alone and metasurface layer in front of slot radiator: a) $|S_{11}|$ and b) FBR c) peak gain.

consequently increases the directivity [27, 42]. The refractive index for the cases when all diodes are ON and all diodes are *OFF* is compared in Fig. 5(c) indicating that the refractive index with the PIN diodes *ON* is smaller than when the PIN diodes are *OFF*. As a result, the main beam can be steered toward the sides by deactivating the PIN diodes based on Snell's law. Moreover, by adjusting the resonance frequency of the unit-cell, the operating bandwidth of the whole structure can be improved.

The gain of any antenna is proportional to its dimensions. Hence, there is a tradeoff between the gain and practical size. In the proposed design, the antenna's dimension is set to cover the human torso. A layer of metasurface that consists of 5×5 unit cells is placed in front of the H-shape radiating slot with a subwavelength air-gap distance of $h_1 = 20$ mm ($0.065\lambda_0$) to increase the bandwidth and FBR of the radiating slot. The distance h_1, controls the gain and back radiation of the antenna. Increasing the parameter h_1, increases the back-lobe radiation due to increasing reflections from the metasurface layer. Conversely, decreasing this distance reduces the number of cells that can be excited by the slot radiator. Consequently, the effective area of the metasurface decreases, leading to a reduction in the antenna directivity. Fig. 6, indicates the effect of adding the metasurface layer on the performance of the antenna. It can be seen that the resonance frequency of the H-shaped radiating slot occurs around 0.9 GHz. The square loop that forms the unit cell of the metasurface structure resonates at its sub-wavelength
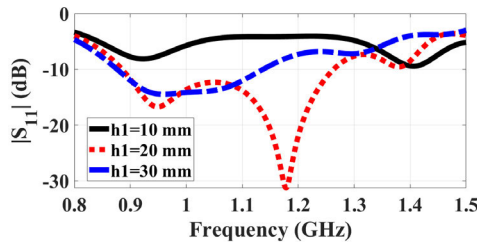
FIGURE 7. Comparison between $|S_{11}|$ for different values of h_1.

resonance at 1.1 GHz. Adding this resonance broadens the operating bandwidth to 30% at 0.9-1.2 GHz (see Fig. 6 (a)). It also increases the FBR value by more than 8 dB across the bandwidth at 0.9-1.2 GHz (see Fig. 6 (b)) and improves the peak gain by more than 5 dB across the operating bandwidth (see Fig. 6(c)). Fig. 7 indicates the impedance matching of the antenna for different values of air-gap height (h_1). As seen, decreasing the h_1 shifts the second resonance caused by metasurface layer to 1.4 GHz, causing a deterioration in the impedance bandwidth at 1-1.3 GHz. Moreover, increasing the air-gap results in narrowing the bandwidth by merging the second resonance with the slot radiator's resonance.

C. BEAM STEERING MECHANISM

The mechanism for switching the radiation beam of the antenna is achieved by selecting different columns or rows of the cells in the metasurface layer (see Fig. 1). By deactivating different columns or rows in the metasurface layer, the electric field distribution on the superstrate layer is altered. Thus, the radiation beam can be directed at designated directions. To get a better understanding of the physical reason behind the beam reconfigurability of the proposed antenna, the electric field distribution of the structure at the center frequency of 1.05 GHz in three different operating *States* is illustrated in Fig. 8. As seen in Fig. 8 (a), in *State I*, when all the cells are activated (all PIN diodes are ON), the high-intensity electric field occurs at the center of the metasurface layer. Thus, the superposition of the radiation from all cells creates a unidirectional pattern, which is maximum at the broadside. On the hand, in *State II*, by deactivating the cells of column #4 and column #5 (Fig. 8 (b)), the electric field intensity shifts towards –x-direction (on azimuth plane (x-z)). So, the adjacent cells are excited with different time delays. As a result, a phase delay is created between adjacent cells leading to a pattern directed at −25° in x-z plane. Similarly, in *State III*, when the left side cells (column #1, and column #2) are deactivated (Fig. 8 (c)), the high-intensity electric field tilts towards the +x direction in the azimuth plane, resulting in a steered beam at +25° in x-z plane.

The generated radiation patterns for different operating *States* at the center frequency of 1.05 GHz are shown in Fig. 9. In can be seen that by switching from *States I* to *State II* and *State III*, the beam is switched from 0° to +25°, and −25° in the azimuth plane, respectively. Due to symmetry of the structure, beam switching in elevation
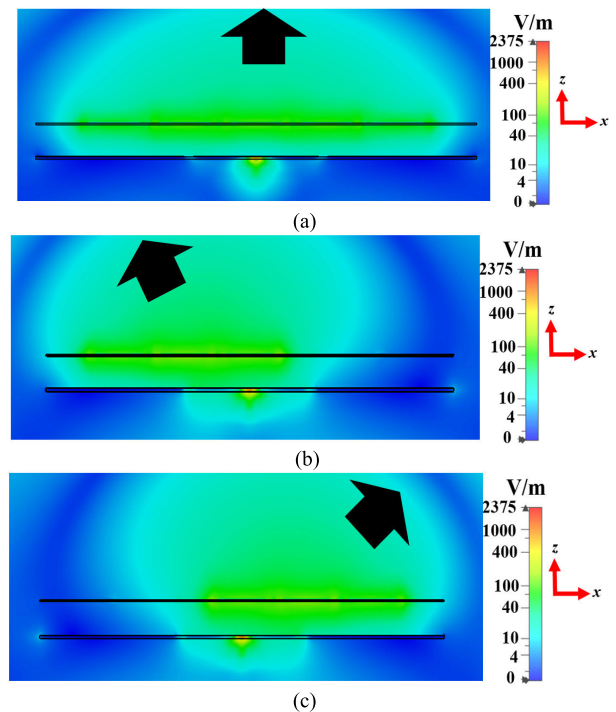

FIGURE 8. Simulated electric field distribution of the antenna at the center frequency of 1.05 GHz for a) *State I*, b) *State II*, and c) *State III*.
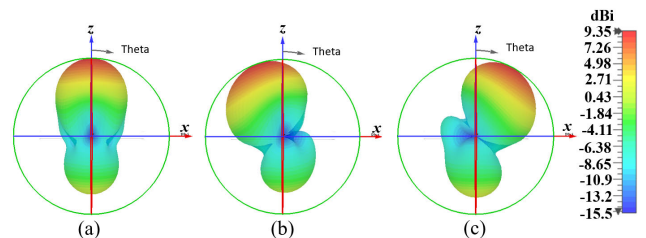

FIGURE 9. Simulated electric field distribution of the antenna at the center frequency of 1.05 GHz for a) *State I*, b) *State II*, and c) *State III*.

plane can also be achieved by deactivating rows #4 and #5 for +y-directed beams, and rows #1 and #2 for -y-directed patterns. Therefore, 2-D beam switching can be achieved using the analysis mentioned above. By utilizing the proposed structure, different beam switching scenarios can be arranged by deactivating different rows and columns. As an example, by deactivating column #5 and column #4 and row #5 and row #4, beam switching along the diagonal of the metasurface is reachable (Fig. 10). To further analyze the capability of the proposed method in steering the radiation patterns, a parametric study on the effect of deactivating each column on the direction of the steered beams is carried out. Fig. 11 (a), depicts the radiation pattern generated at the center frequency of 1.05 GHz by selecting different columns of cells. Studying Fig. 11 (a), reveals that by switching between different columns of active cells. Radiation pattern can be switched from −25° (column #4 and column #5 deactivated) to −15° (column #5 deactivated), 0° (all cells are active), +15° (column #2 deactivated), and +25° (column #1 and column #2
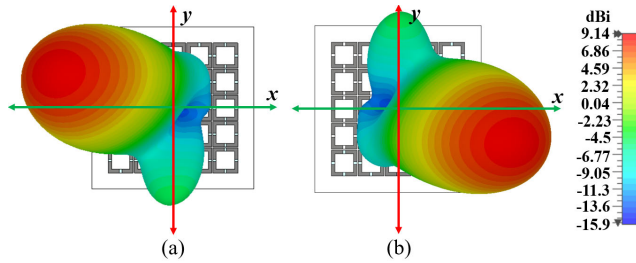
FIGURE 10. Pattern reconfigurability along the diagonal of the metasurface at the center frequency of 1.05 GHz: a) deactivating column #5 and column #4 and row #5 and row #4, and b) deactivating column #1 and column #2 and row #1 and row #2.
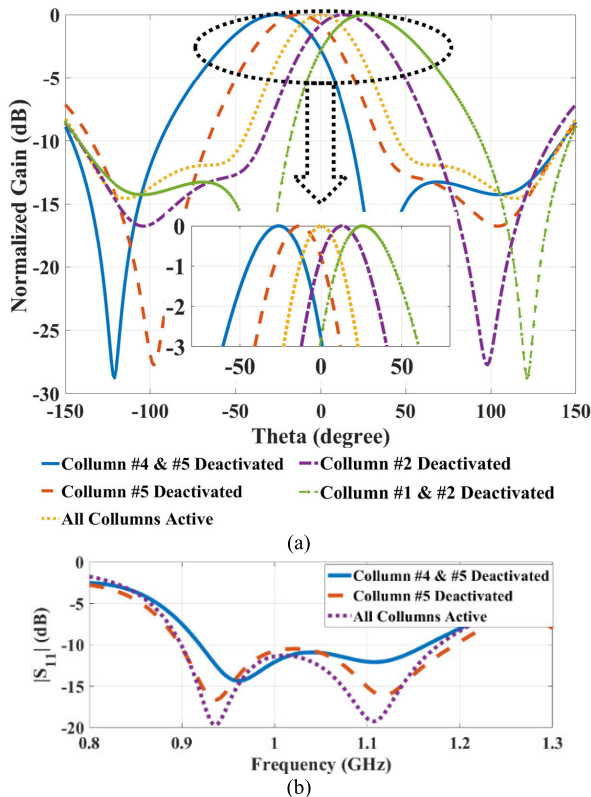

(a)

(b)

FIGURE 11. Pattern reconfigurability along the diagonal of the metasurface: a) deactivating column #5 and column #4 and row #5 and row #4, and b) deactivating column #1 and column #2 and row #1 and row #2.

deactivated) in the azimuth (x-z) plane. Similarly, the radiation pattern can be steered in the elevation plane towards $-25°$ (deactivating row#1 and row#2), $-15°$(deactivating row#1), $0°$ (activating all cells), $+15°$ (deactivating row#5), and $+25°$ (deactivating row#4 and row#5). The impedance matching variations of the antenna for different operating *States* are shown in Fig. 11 (b). By deactivating each column, the second resonance of the antenna, which is related to the metasurface layer becomes weaker. Yet, the antenna still maintains its wideband performance within the operational bandwidth of 0.9 GHz-1.2 GHz for all operating *States*.

D. DC-CONTROLLING CIRCUIT
In a radar-based EMI systems, the antenna is located at a close distance from the body, e.g. 10 cm, to achieve the
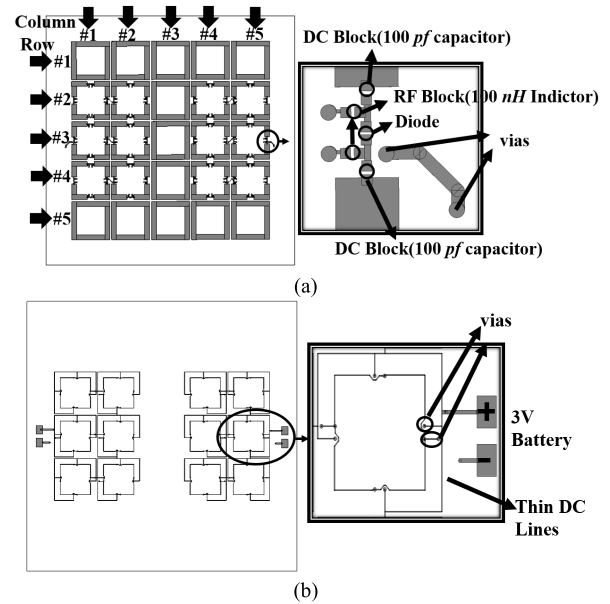

(a)

(b)

FIGURE 12. DC-biasing circuit: (a) top, and (b) rear views.

required penetration [43]. Considering the size of a normal torso, antenna's radiation beam width and its distance from the scanning region, a beam switching antenna with the steering capability of $\pm25°$ steps can scan whole torso area. Hence, an antenna is fabricated and measured. To facilitate the switching between different states, the conventional series single pole single throw (SPST) DC-Biasing circuit for the diodes controlling the cells is designed using 100 *pF* capacitors as DC blocks and 100 *nH* inductors as RF blocks (see Fig. 12 (a). The DC blocking capacitors act as a high pass filter to block DC from the signal path and allow the high frequency signals to be passed. At the operating band of higher than 0.5 GHz, these capacitors acts as short circuits. The surface mount MA4SPS402 diodes with low parasitic capacitance and inductance are used. The total capacitance of this diode including the junction and parasitic capacitors has the typical value of 0.055 *pF*, which is applied to the simulated CST lumped element model of the diode. A pair of thin DC-lines are designed at the back of the metasurface layer to avoid RF/DC interference. These lines form a series combination of all the diodes used in the cells of column #5 and column #6. These lines are connected to a 3 *Volt* battery (see Fig. 12 (b)). Via holes are used to transfer the biasing lines to the back of the metasurface layer for a better access to the biasing circuits. Similarly, the left side cells (column #1 & #2) are controlled using another 3 *Volt* battery.

To simplify the biasing network and minimize the effect of the DC biasing lines on the performance, the diodes at the row#1, row#2, and column#3 are removed from the unit cells. Then, the final antenna, with all the DC lines, capacitors and inductors, is simulated in CST Microwave Studio. The dimensions of the antenna were slightly tuned to alleviate the adverse effect of the biasing network on the antenna's performance. The final dimensions of the antenna are presented in
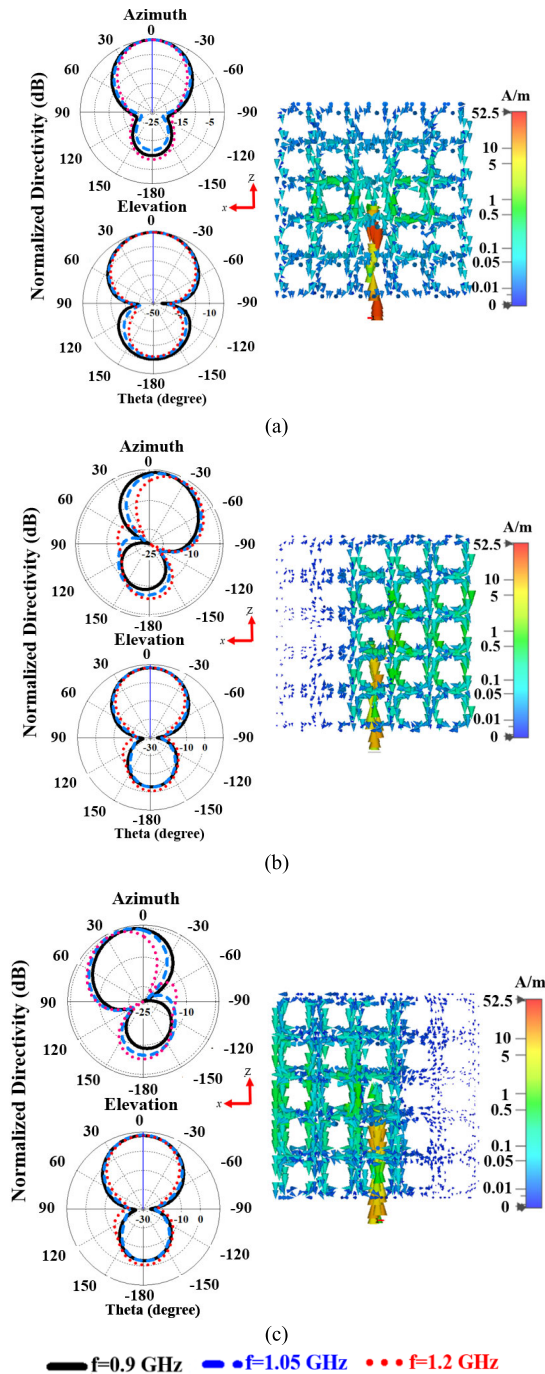
(a)

(b)

(c)

━━ f=0.9 GHz   ●━● f=1.05 GHz   • • • f=1.2 GHz

FIGURE 13. Simulated radiation patterns (left) and associated simulated surface current distribution (right) of the antenna at 0.9 GHz, 1.05 GHz, and 1.2 GHz for (a) *State I*, (b) *State II*, and (c) *State III*.

Fig. 1. The generated radiation patterns and associated surface currents of the antenna at three frequencies of 0.9 GHz, 1.05 GHz and 1.2 GHz for three different operating *States* are presented in Fig. 13. Analyzing the surface currents reveal that when all the diodes are activated, the superposition of the radiation from all cells results in high electromagnetic intensity towards the center of the metasurface layer, leading to a focused beam at the center (0° in x-z (azimuth) plane).
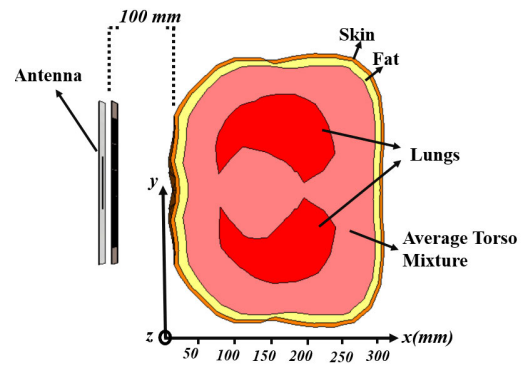

FIGURE 14. Antenna in front of a human torso phantom (top view).

By deactivating diodes of the left side cells, an asymmetric surface contribution across the metasurface is created, leading to strong radiation from the right side of the surface compared to the left side. Consequently, the beam is steered towards −25° in x-z (azimuth) plane (see Fig. 13 (b)). To switch the beam to +25° (Fig. 13 (c)), the right-side diodes are deactivated. Therefore, the majority of the radiated power is radiated by the left side cells. As a result, the beam is directed at +25° on x-z (azimuth) plane. Thus, the antenna is capable of switching the radiation pattern from −25° to 0° and to +25° across wide fractional bandwidth of 30% at the center frequency of 1.05 GHz in the azimuth plane, whereas the beam is stable in the elevation plane. Moreover, studying the radiation patterns presented in Fig. 13 indicates that the antenna remains its beam switching performance despite removing the diodes from the unit cells in the row#1, row#2, and column #3.

E. ANTENNA IN FRONT OF THE HUMAN TORSO

The proposed metasurface structure for reconfiguring the beam of the antenna can be used in different fields of telecommunication engineering such as wireless communication and radar applications, in addition to medical imaging. To investigate the effectiveness of the proposed antenna in an EMI system, it is placed at a 10 cm distance from a torso phantom and is simulated in CST Microwave Studio software (Fig. 14). The 3-D human torso model (Ansys EMAG human body model) [44], is extracted from MRI images with 1 mm resolution. It includes skin, fat, and lungs. The frequency dispersive properties of each tissue are considered in the simulation [45]. The average electric field intensity inside torso with and without metasurface layer at the center frequency of 1.05 GHz is compared in Fig. 15. Analyzing Fig. 15, reveals that the intensity of the electric field can be improved up to 7 dB inside the torso at x = 100 mm using metasurface layer. The electric field intensity inside the torso model for different operating *States* at the center frequency of 1.05 GHz is calculated and illustrated in Fig. 16. As seen, by switching between different beam directions, the peak electric field intensity is switched inside the human chest. In *State I*, the
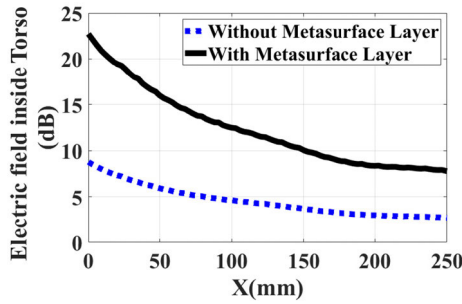
FIGURE 15. Electric field density inside the torso at the center frequency of 1.05 GHz.
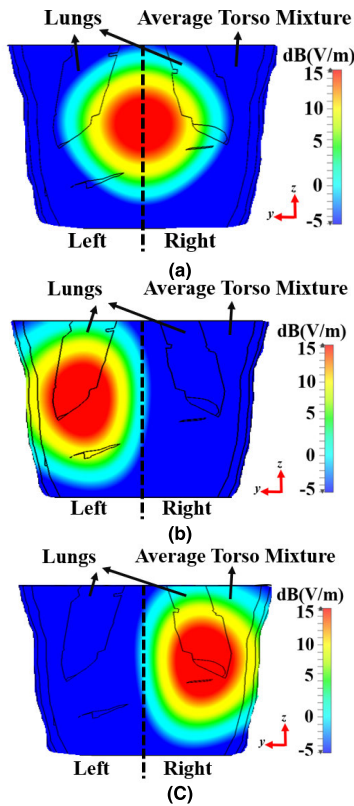

FIGURE 16. Electric field density inside the torso at the center frequency of 1.05 GHz. a) *State I* a) *State II*, and b) *State III*.

FIGURE 17. $|S_{11}|$ comparison of the antenna in free space and in front of the human torso phantom.
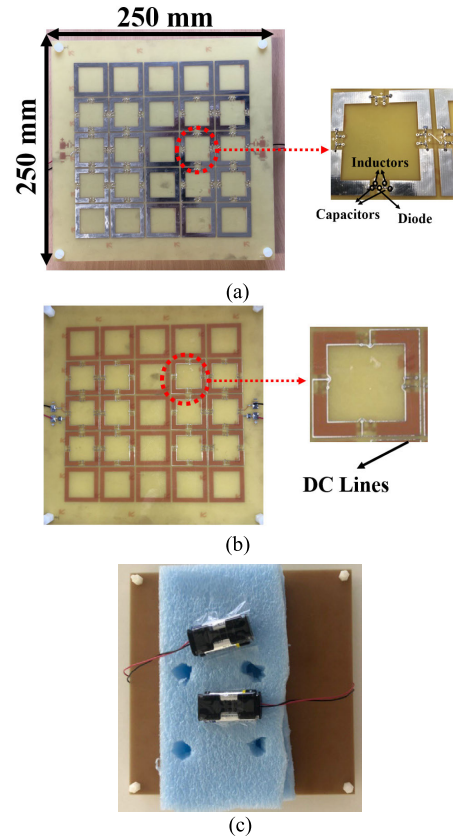
FIGURE 18. Fabricated antenna, a) top view, b) DC-lines, and c) bottom view and batteries.

maximum of the electric field inside the torso occurs at the center. However, by switching to operating *States II & III*, the intensity of the electric field is changed toward the left and right areas, respectively. Thus, without mechanically moving the antenna position, different positions across the whole torso area can be scanned electronically. Fig. 17, compares the $|S_{11}|$ characteristic of the antenna in free space and in front of the human phantom for *State I* operating mode. Analyzing Fig. 17, reveals that despite the loading effect of the torso, the antenna retains its wideband operation at 0.9-1.2 GHz. It should be noted that the differences between the signals in free space and in front of the torso are then utilized to detect the abnormalities inside the torso. Decreasing the distance between the antenna and the human torso worsens
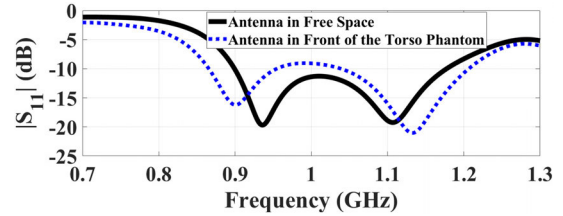
the impedance matching and bandwidth, while it improves the signal penetration. Simulating the antenna at different distances from the torso phantom model reveals that the distance 100 mm has the best compromise between the impedance matching and signal penetration into the human body.

III. FABRICATION AND MEASUREMENT

Fig. 18 depicts the photograph of antenna. To reduce the adverse effects of batteries on the performance, they were located at the back of the antenna. Fig. 19 compares the simulated and measured reflection coefficients of the antenna for three different operating *States*. There is a reasonable agreement between simulated and measured results with discrepancies caused by biasing circuit and fabrication errors. The measured patterns for three different operating *States* at three operating frequency samples of 0.9 GHz, 1.05 GHz,
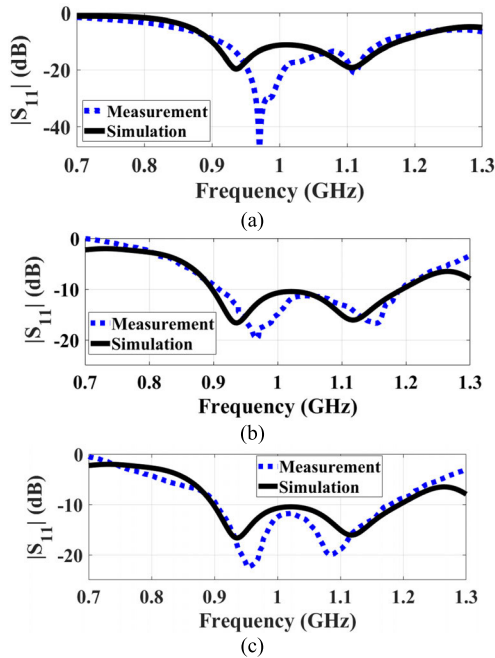
FIGURE 19. Simulated and measured |S₁₁| for different operating *States*: a) *State I*, b) *State II*, and c) *State III*.

TABLE 1. Measured and simulated gain at different frequencies.

Freq. (GHz)	Gain(dBi)- *State* I		Gain(dBi)- *State* II		Gain(dBi)- *State* III	
	Sim.	Meas.	Sim.	Meas.	Sim.	Meas.
0.9	8.9	8.5	8.5	8.1	8.5	7.8
1.05	9.2	8.6	9	8.4	9	8.4
1.2	9.6	9.4	9.4	9.2	9.4	9.3

FIGURE 20. Measured azimuth radiation patterns at a) 0.9 GHz, b) 1.05 GHz, and c) 1.2 GHz.

and 1.2 GHz are presented in Fig. 20. In *State I*, both of the left and right-side batteries are connected. So, all cells are activated and as illustrated in Fig. 19 (a), the antenna has a measured operating bandwidth from 0.9 GHz to 1.2 GHz. As can be seen from Fig. 20, the radiation pattern directed at 0°. By switching to *State II*, the right-side battery is disconnected from the circuit, deactivating cells in column #5 and column #6. As seen in Fig. 19 (b), the antenna maintains its wide operational bandwidth, and the beam is directed at −25° in x-z plane. Similarly, by disconnecting the right-side battery, the diodes in cells of columns #1 & #2 are deactivated and the beam is directed at +25° in x-z plane. The gain of antenna for three operating States was measured in an anechoic chamber and the results are presented in Table 1. The antenna has a peak measured gain of 9.4 dBi, for the center beam at the frequency of 1.2 GHz with 1.5 dB gain variations across the operating bandwidth.

To investigate the performance of the antenna in an electromagnetic scanning system, the antenna is placed at the distance of 10 cm in front of a human phantom (see Fig. 21). The system is surrounded with absorbers to reduce the effect of the environment on the results. The utilized 3-D phantom contains ski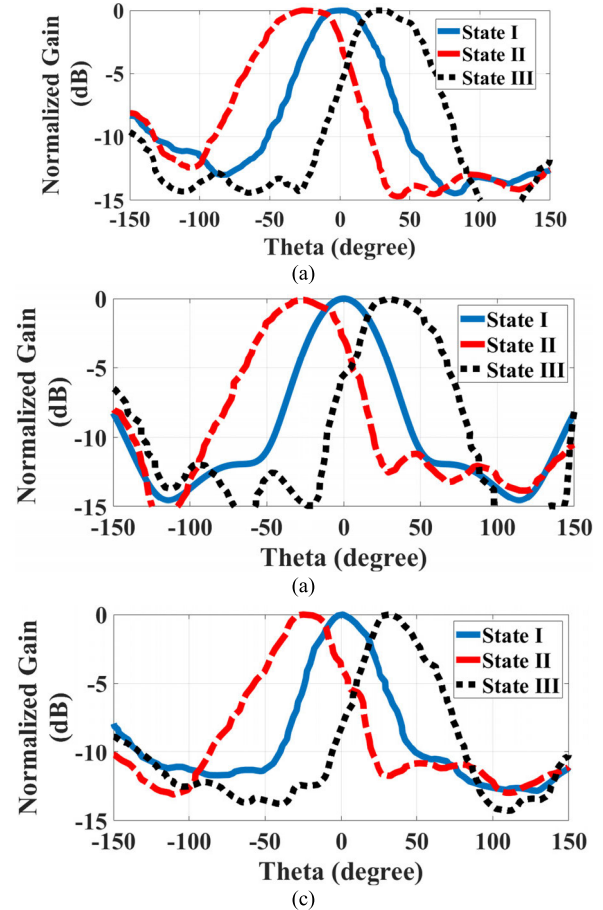n and fat, and is filled with tissue-mimicking liquid to represent the average dielectric properties of the human torso ($\varepsilon_r = 40$ at 1 GHz). This phantom is water-based with the realistic dimensions of an average human torso. An electric field probe that is connected to a field fox vector network analyzer is used to collect S₂₁ signals inside the torso phantom (y=-100 mm). The data acquisition involves displacing the electric probe along x-direction between −200mm (left side) to 200mm (right side) with 25 mm step sizes. This process is performed in three vertical positions at z= 0, 50mm and -50 mm. The acquired data is then used to calculate the electric field distribution of the antenna inside the torso phantom for different operating *States*. Fig. 22 depicts the intensity of electric field distribution inside the torso phantom at the center operating frequency of 1.05 GHz for different operating *States*. As seen, by switching between the operating *State II*, to *State I*, and *State III*, the intensity of the electric field switches from left side of torso towards center and right side, respectively without mechanically moving the antenna. The scanning depth of the antenna is related to the minimum detectable signal of the VNA. Considering the noise level of the VNA used in the measurement (−90 dB), the depth of 150 mm (y = −150 mm) is scannable using this metasurface antenna.

TABLE 2. Comparison with pervious works.

| Paper	BW (% @ Center Freq)	Dimensions ($\lambda_0 \times \lambda_0 \times \lambda_0$) λ_0 @ Center Freq	Max Scan Angle (^{0})	Max Gain (dBi)	Beam-Switching Technique
[25]	3.8 % (@2 GHz)	$2.3\lambda_0 \times 2.3\lambda_0 \times 0.52\lambda_0$	$\pm10^0$	13	Varactor diodes
[26]	4 % (@5.5 GHz)	$3.1\lambda_0 \times 3.1\lambda_0 \times 0.55\lambda_0$	$\pm15^0$	12	PIN diodes
[29]	4.1 % (@ 5.5 GHz)	$0.6\lambda_0 \times 0.6\lambda_0 \times 0.05\lambda_0$	$\pm32^0$	7.2	Mechanically
[30]	3.8 % (@ 2.6 GHz)	$1.04\lambda_0 \times 1.04\lambda_0 \times 0.06\lambda_0$	$\pm20^0$	5.7	Water
[31]	5.8 %(@10.4 GHz)	$11.2\lambda_0 \times 11.2\lambda_0$	$\pm18.3^0$	25	PIN diodes
[32]	3.77%(@26.5 GHz)	$3.7\lambda_0 \times 3.7\lambda_0$	40^0	11.42	MEMS switches
This work	30 % (@ 1.05 GHz)	$0.9\lambda_0 \times 0.9\lambda_0 \times 0.06\lambda_0$	$\pm25^0$	9.4	PIN diodes
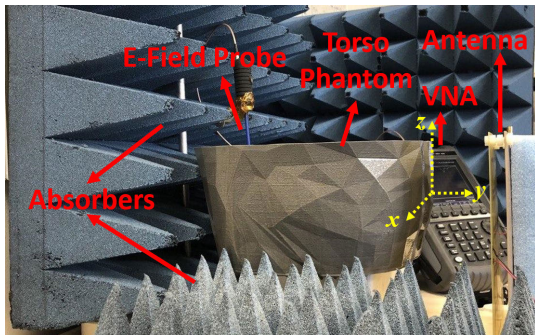
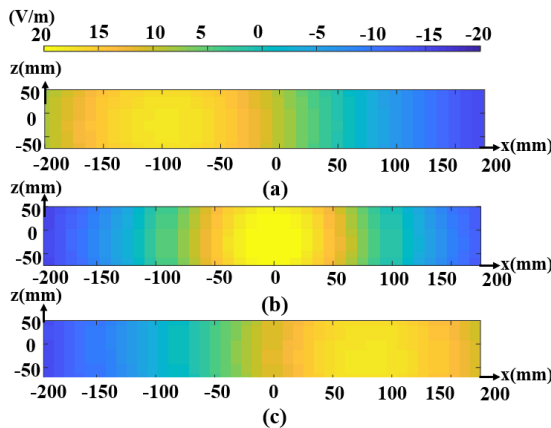**FIGURE 21.** Electric field measurement inside the torso phantom.

FIGURE 22. Measured electric field density inside the torso at the center frequency of 1.05 GHz. a) *State II* a) *State I*, and b) *State III*.

To evaluate the performance of the proposed design, it is compared to some recent reconfigurable designs in terms of operating bandwidth, dimension, beam scanning capability, maximum gain and the utilized beam switching technique. As seen from Table 2, the proposed antenna achieves wider bandwidth and reasonably compact dimensions compared to [25], [26], [31], [32]. Additionally, it offers faster beam switching compared to the mechanical switching [29] and programmable water injection techniques [30]. Moreover, the proposed method offers higher degrees of freedom in the number of switchable beam/modes. The proposed design is capable of switching the beam at both azimuth and elevation planes besides providing reconfigurability on diagonal directions. The mechanism of beam switching in the proposed design is based on altering the electric field intensity on the superstrate layer by activating/deactivating the unit cells. Consequently, the DC-biasing circuit can form a series combination of all diodes, enabling the circuit to be simpler compared to pattern reconfigurable reflectarrays.
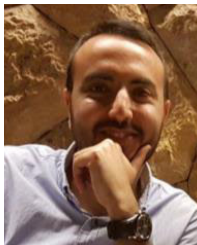
IV. CONCLUSION

A compact wideband pattern reconfigurable metasurface antenna that can be potentially used for electromagnetic scanning systems has been presented. An H-shape radiating slot is designed to feed a metasurface layer, which consists of 5 rows and 5 columns of square ring resonator unit cells to cover the human chest area. By deactivating different columns and rows of the cells using PIN diodes, the concentration of the electric field across the metasurface is altered. The generated beams are then steered towards designated directions. Pattern reconfigurability in the azimuth plane, elevation plane and diagonal axis of the superstrate metasurface layer is achieved. The proposed antenna achieves a measured fractional bandwidth of 30% (0.9-1.2 GHz) and is able to switch the radiation pattern from $-25°$ to $0°$, and $+25°$ with peak gain of 9.5 dBi. The antenna is successfully tested to steer the electric field inside a torso phantom.

REFERENCES

[1] *Fluid in the Chest (Pleural Effusion)*. Accessed: Jan. 1, 2020. [Online]. Available: https://www.healthline.com/health/pleural-effusion

[2] S. Salman, Z. Wang, E. Colebeck, A. Kiourti, E. Topsakal, and J. L. Volakis, "Pulmonary edema monitoring sensor with integrated body-area network for remote medical sensing," *IEEE Trans. Antennas Propag.*, vol. 62, no. 5, pp. 2787–2794, May 2014.

[3] S. A. Rezaeieh, A. Zamani, K. S. Bialkowski, and A. M. Abbosh, "Novel microwave torso scanner for thoracic fluid accumulation diagnosis and monitoring," *Sci. Rep.*, vol. 7, no. 1, p. 304, Dec. 2017, doi: 10.1038/s41598-017-00436-w.

[4] S. Zhang, G. Xu, X. Zhang, B. Zhang, H. Wang, Y. Xu, N. Yin, Y. Li, and W. Yan, "Computation of a 3-D model for lung imaging with electrical impedance tomography," *IEEE Trans. Magn.*, vol. 48, no. 2, pp. 651–654, Feb. 2012, doi: 10.1109/TMAG.2011.2174779.

[5] D. Kurrant, J. Bourqui, C. Curtis, and E. Fear, "Evaluation of 3-D acquisition surfaces for radar-based microwave breast imaging," *IEEE Trans. Antennas Propag.*, vol. 63, no. 11, pp. 4910–4920, Nov. 2015, doi: 10.1109/TAP.2015.2476415.

[6] M. R. Casu, M. Vacca, J. A. Tobon, A. Pulimeno, I. Sarwar, R. Solimene, and F. Vipiana, "A COTS-based microwave imaging system for breast-cancer detection," *IEEE Trans. Biomed. Circuits Syst.*, vol. 11, no. 4, pp. 804–814, Aug. 2017, doi: 10.1109/TBCAS.2017.2703588.

[7] A. Abbosh, "Electromagnetic medical sensing," *Sensors*, vol. 19, no. 7, p. 1662, Apr. 2019. [Online]. Available: https://www.mdpi.com/1424-8220/19/7/1662

[8] M. Persson, A. Fhager, H. D. Trefna, Y. Yu, T. McKelvey, G. Pegenius, J.-E. Karlsson, and M. Elam, "Microwave-based stroke diagnosis making global prehospital thrombolytic treatment possible," *IEEE Trans. Biomed. Eng.*, vol. 61, no. 11, pp. 2806–2817, Nov. 2014, doi: 10.1109/TBME.2014.2330554.

[9] A. Modiri, S. Goudreau, A. Rahimi, and K. Kiasaleh, "Review of breast screening: Toward clinical realization of microwave imaging," *Med. Phys.*, vol. 44, no. 12, pp. e446–e458, Dec. 2017, doi: 10.1002/mp.12611.

[10] S. A. Rezaeieh, Y.-Q. Tan, A. Abbosh, and M. A. Antoniades, "Equivalent circuit model for finding the optimum frequency range for the detection of heart failure using microwave systems," in *Proc. IEEE Antennas Propag. Soc. Int. Symp. (APSURSI)*, Jul. 2013, pp. 2059–2060.

[11] A. Zamani, A. M. Abbosh, and A. T. Mobashsher, "Fast frequency-based multistatic microwave imaging algorithm with application to brain injury detection," *IEEE Trans. Microw. Theory Techn.*, vol. 64, no. 2, pp. 653–662, Feb. 2016, doi: 10.1109/TMTT.2015.2513398.

[12] M. Rokunuzzaman, M. Samsuzzaman, and M. T. Islam, "Unidirectional wideband 3-D antenna for human head-imaging application," *IEEE Antennas Wireless Propag. Lett.*, vol. 16, pp. 169–172, 2017.

[13] M. Abbak, M. N. Akinci, M. Cayoren, and I. Akduman, "Experimental microwave imaging with a novel corrugated Vivaldi antenna," *IEEE Trans. Antennas Propag.*, vol. 65, no. 6, pp. 3302–3307, Jun. 2017, doi: 10.1109/TAP.2017.2670228.

[14] A. Sabouni and A. A. Kishk, "Dual-polarized, broadside, thin dielectric resonator antenna for microwave imaging," *IEEE Antennas Wireless Propag. Lett.*, vol. 12, pp. 380–383, 2013, doi: 10.1109/LAWP.2013.2252142.

[15] S. A. Rezaeieh, M. A. Antoniades, and A. M. Abbosh, "Miniaturization of planar Yagi antennas using mu-negative metamaterial-loaded reflector," *IEEE Trans. Antennas Propag.*, vol. 65, no. 12, pp. 6827–6837, Dec. 2017, doi: 10.1109/TAP.2017.2758174.

[16] M. T. Islam, M. Samsuzzaman, S. Kibria, N. Misran, and M. T. Islam, "Metasurface loaded high gain antenna based microwave imaging using iteratively corrected delay multiply and sum algorithm," *Sci. Rep.*, vol. 9, no. 1, p. 17317, Dec. 2019, doi: 10.1038/s41598-019-53857-0.

[17] M. T. Islam, M. Samsuzzaman, M. T. Islam, S. Kibria, and M. J. Singh, "A homogeneous breast phantom measurement system with an improved modified microwave imaging antenna sensor," *Sensors*, vol. 18, no. 9, p. 2962, Sep. 2018.

[18] S. A. Rezaeieh, A. Zamani, K. Bialkowski, G. Macdonald, and A. Abbosh, "Three-dimensional electromagnetic torso scanner," *Sensors*, vol. 19, no. 5, p. 1015, Feb. 2019. [Online]. Available: https://www.mdpi.com/1424-8220/19/5/1015

[19] A. Darvazehban, O. Manoochehri, M. A. Salari, P. Dehkhoda, and A. Tavakoli, "Ultra-wideband scanning antenna array with Rotman lens," *IEEE Trans. Microw. Theory Techn.*, vol. 65, no. 9, pp. 3435–3442, Sep. 2017.

[20] P. I. Bantavis, C. I. Kolitsidas, T. Empliouk, M. Le Roy, B. L. G. Jonsson, and G. A. Kyriacou, "A cost-effective wideband switched beam antenna system for a small cell base station," *IEEE Trans. Antennas Propag.*, vol. 66, no. 12, pp. 6851–6861, Dec. 2018, doi: 10.1109/TAP.2018.2874494.

[21] H.-T. Chou and Z.-D. Yan, "Parallel-plate Luneburg lens antenna for broadband multibeam radiation at millimeter-wave frequencies with design optimization," *IEEE Trans. Antennas Propag.*, vol. 66, no. 11, pp. 5794–5804, Nov. 2018, doi: 10.1109/TAP.2018.2867060.

[22] O. Manoochehri, A. Darvazehban, M. A. Salari, A. Emadeddin, and D. Erricolo, "A parallel plate ultrawideband multibeam microwave lens antenna," *IEEE Trans. Antennas Propag.*, vol. 66, no. 9, pp. 4878–4883, Sep. 2018, doi: 10.1109/TAP.2018.2845548.

[23] S. Liu, K. Jiang, G. Xu, X. Ding, K. Zhang, J. Fu, and Q. Wu, "A dual-band shared aperture antenna array in Ku/Ka-bands for beam scanning applications," *IEEE Access*, vol. 7, pp. 78794–78802, 2019, doi: 10.1109/ACCESS.2019.2922647.

[24] J. G. Lee, T. H. Jang, G. H. Park, H. S. Lee, C. W. Byeon, and C. S. Park, "A 60-GHz four-element beam-tapering phased-array transmitter with a phase-compensated VGA in 65-nm CMOS," *IEEE Trans. Microw. Theory Techn.*, vol. 65, no. 7, pp. 2998–3009, Jul. 2019, doi: 10.1109/TMTT.2019.2907242.

[25] T. Debogovic and J. Perruisseau-Carrier, "Array-fed partially reflective surface antenna with independent scanning and beamwidth dynamic control," *IEEE Trans. Antennas Propag.*, vol. 62, no. 1, pp. 446–449, Jan. 2014.

[26] L.-Y. Ji, Y. J. Guo, P.-Y. Qin, S.-X. Gong, and R. Mittra, "A reconfigurable partially reflective surface (PRS) antenna for beam steering," *IEEE Trans. Antennas Propag.*, vol. 63, no. 6, pp. 2387–2395, Jun. 2015.

[27] T. Hongnara, S. Chaimool, P. Akkaraekthalin, and Y. Zhao, "Design of compact beam-steering antennas using a metasurface formed by uniform square rings," *IEEE Access*, vol. 6, pp. 9420–9429, 2018, doi: 10.1109/ACCESS.2018.2799551.

[28] A. Darvazehban, S. A. Rezaeieh, A. Zamani, and A. M. Abbosh, "Pattern reconfigurable metasurface antenna for electromagnetic torso imaging," *IEEE Trans. Antennas Propag.*, vol. 67, no. 8, pp. 5453–5462, Aug. 2019, doi: 10.1109/TAP.2019.2916576.

[29] H. L. Zhu, T. I. Yuk, and S. W. Cheung, "Mechanically pattern reconfigurable antenna using metasurface," *IET Microw., Antennas Propag.*, vol. 9, no. 12, pp. 1331–1336, Sep. 2015, doi: 10.1049/iet-map.2014.0676.

[30] A. H. Naqvi and S. Lim, "A beam-steering antenna with a fluidically programmable metasurface," *IEEE Trans. Antennas Propag.*, vol. 67, no. 6, pp. 3704–3711, Jun. 2019, doi: 10.1109/TAP.2019.2905690.

[31] E. Carrasco, M. Barba, and J. A. Encinar, "X-band reflectarray antenna with switching-beam using PIN diodes and gathered elements," *IEEE Trans. Antennas Propag.*, vol. 60, no. 12, pp. 5700–5708, Dec. 2012, doi: 10.1109/TAP.2012.2208612.

[32] O. Bayraktar, O. A. Civi, and T. Akin, "Beam switching reflectarray monolithically integrated with RF MEMS switches," *IEEE Trans. Antennas Propag.*, vol. 60, no. 2, pp. 854–862, Feb. 2012, doi: 10.1109/TAP.2011.2173099.

[33] F. Venneri, S. Costanzo, and G. Di Massa, "Design and validation of a reconfigurable single varactor-tuned reflectarray," *IEEE Trans. Antennas Propag.*, vol. 61, no. 2, pp. 635–645, Feb. 2013, doi: 10.1109/TAP.2012.2226229.

[34] W. Li, Z. Xia, B. You, Y. Liu, and Q. H. Liu, "Dual-polarized H-shaped printed slot antenna," *IEEE Antennas Wireless Propag. Lett.*, vol. 16, pp. 1484–1487, 2017, doi: 10.1109/LAWP.2016.2646805.

[35] D. Byrne and I. J. Craddock, "Time-domain wideband adaptive beamforming for radar breast imaging," *IEEE Trans. Antennas Propag.*, vol. 63, no. 4, pp. 1725–1735, Apr. 2015, doi: 10.1109/TAP.2015.2398125.

[36] N. Ghavami, G. Tiberi, D. J. Edwards, and A. Monorchio, "Microwave imaging through a mode-matching Bessel functions procedure," *IEEE Trans. Microw. Theory Techn.*, vol. 61, no. 8, pp. 2753–2760, Aug. 2013, doi: 10.1109/TMTT.2013.2271612.

[37] Q. Rao, T. A. Denidni, and R. H. Johnston, "A new aperture coupled microstrip slot antenna," *IEEE Trans. Antennas Propag.*, vol. 53, no. 9, pp. 2818–2826, Sep. 2005, doi: 10.1109/TAP.2005.854521.

[38] J. R. James, *Handbook of Microstrip Antennas*. Edison, NJ, USA: IET, 1989.

[39] D. M. Pozar and S. D. Targonski, "Improved coupling for aperture coupled microstrip antennas," *Electron. Lett.*, vol. 27, no. 13, pp. 1129–1131, Jun. 1991, doi: 10.1049/el:19910705.

[40] K. R. Jha, G. Singh, and R. Jyoti, "A simple synthesis technique of single-square-loop frequency selective surface," *Prog. Electromagn. Res. B*, vol. 45, pp. 165–185, Oct. 2012.

[41] X. Chen, T. M. Grzegorczyk, B.-I. Wu, J. Pacheco, and J. A. Kong, "Robust method to retrieve the constitutive effective parameters of metamaterials," *Phys. Rev. E, Stat. Phys. Plasmas Fluids Relat. Interdiscip. Top.*, vol. 70, no. 1, Jul. 2004, Art. no. 016608.

[42] S. Chaimool, C. Rakluea, and P. Akkaraekthalin, "Mu-near-zero metasurface for microstrip-fed slot antennas," *Appl. Phys. A, Solids Surf.*, vol. 112, no. 3, pp. 669–675, Sep. 2013.

[43] S. A. Rezaeieh, A. Abbosh, and Y. Wang, "Wideband unidirectional antenna of folded structure in microwave system for early detection of congestive heart failure," *IEEE Trans. Antennas Propag.*, vol. 62, no. 10, pp. 5375–5381, Oct. 2014.

[44] M. Horner. *Human Body Modeling With ANSYS Software*. Accessed: Mar. 1, 2020. [Online]. Available: https://support.ansys.com/staticassets/ANSYS/Conference/Minnesota/downloads/Human%20Body%20Modeling%20ANSYS%20Software.pdf

[45] P. A. Hasgall, F. Di Gennaro, C. Baumgartner, E. Neufeld, B. Lloyd, M. C. Gosselin, D. Payne, A. Klingenböck, and N. Kuster, "IT'IS database for thermal and electromagnetic parameters of biological tissues, version 4.0," Found. Res. Inf. Technol. Soc. (IT'IS), Zürich, Switzerland, May 2018. [Online]. Available: http://itis.swiss/database, doi: 10.13099/VIP21000-04-0.

SASAN AHDI REZAEIEH (Member, IEEE) received the Ph.D. degree from The University of Queensland, Brisbane, QLD, Australia, in 2016, with a focus on design of electromagnetic torso scanner systems. His current research interests include design and miniaturization of several types of metamaterial, metasurface, and pattern reconfigurable antennas for electromagnetic medical diagnostic systems. He was a recipient of the IEEE Antennas and Propagation Society Doctoral Research Award in 2014, the IEEE Antennas and Propagation Letters Outstanding Reviewer Award in 2018, and the Prestigious Advance Queensland Fellowship jointly funded by the Queensland Government, Australia, and The University of Queensland.

AMIN DARVAZEHBAN (Student Member, IEEE) received the B.Sc. degree in electrical engineering from Shahid Beheshti University, Tehran, Iran, in 2011, and the M.S. degree from the Amirkabir University of Technology, Tehran, Iran, in 2013. He is currently pursuing the Ph.D. degree with the Electromagnetic Innovations (εMAGin) Group, School of Information Technology and Electrical Engineering, University of Queensland, Australia.

He was a Researcher with the Electromagnetic and Nondestructive Testing Laboratory, Amirkabir University of Technology, from 2013 to 2017. His current research interests include the design of various miniaturized biomedical antennas, beam forming networks, metasurfaces, pattern reconfigurable antennas, and passive microwave devices.

AMIN M. ABBOSH (Senior Member, IEEE) received the D.Eng. degree from The University of Queensland (UQ), Brisbane, QLD, Australia, in 2013. He leads the Electromagnetic Innovations (εMAGin) Group, UQ, where he is the Head of the School of Information Technology and Electrical Engineering. He has authored more than 400 articles on electromagnetic imaging systems for medical applications, wideband passive microwave devices, and planar antennas. He received the UQ's Excellence in Supervision in 2016 for his leading role in mentioning Ph.D. students. He is an Associate Editor of the IEEE TRANSACTIONS ON ANTENNAS AND PROPAGATION and the Senior Associate Editor of the IEEE ANTENNAS AND WIRELESS PROPAGATION LETTERS.

• • •